

Numerical Simulation of Magnetic Nano Drug Targeting in Patient-Specific Lower Respiratory Tract [☆]

Flavia Russo^a, Andrea Boghi^{b,*}, Fabio Gori^a

^a*Department of Mechanical Engineering, University of Rome "Tor Vergata", Via del politecnico 1, 00133 Rome, Italy*

^b*School of Water, Energy and Environment, Cranfield University, Cranfield, Bedfordshire MK43 0AL, United Kingdom*

Abstract

Magnetic nano drug targeting, with an external magnetic field, can potentially improve the drug absorption in specific locations of the body. However, the effectiveness of the procedure can be reduced due to the limitations of the magnetic field intensity. This work investigates this technique with the Computational Fluid Dynamics (CFD) approach. A single rectangular coil generates the external magnetic field. A patient-specific geometry of the Trachea, with its primary and secondary bronchi, is reconstructed from Digital Imaging and Communications in Medicine (DICOM) formatted images, throughout the Vascular Modelling Tool Kit (VMTK) software. A solver, coupling the Lagrangian dynamics of the magnetic nanoparticles with the Eulerian dynamics of the air, is used to perform the simulations. The resistive pressure, the pulsatile inlet velocity and the rectangular coil magnetic field are the boundary conditions. The dynamics of the injected particles is investigated without and with the magnetic probe. The flow field promotes particles adhesion to the tracheal wall. The particles volumetric flow rate in both cases has been calculated. The magnetic probe is shown to increase the particles flow in the target region, but at a limited extent. This behavior has been attributed to the small particle size and the probe configuration.

Keywords: Magnetic Hydro Dynamics, Patient-Specific, nanoparticles, Lagrangian model, Eulerian model, Lower respiratory tract.

1. Introduction

The lung cancer, a malignant tumor, is the first cause of death among common cancers, with the World Health Organization reporting a number of death of 1.5 million during 2012 [1]. The disease strikes mainly men, 16.7% of the

[☆]Nano Drug Targeting in Lower Respiratory Tract

*A. Boghi

Email address: a.boghi@cranfield.ac.uk (Andrea Boghi)

5 total, with the highest estimated age-standardized incidence rate in Central,
6 Eastern Europe and Eastern Asia. The incidence is lower among women, with
7 the highest estimated rates in Northern America and Northern Europe [2]. It
8 appears impossible to prevent this disease, although the incidence can be re-
9 duced by avoiding the main risk factors, such as smoking and air pollution.
10 Treatment and long term outcomes rely on the type of cancer, the stage when
11 is treated and the patients health. Chemotherapy, surgery and radiotherapy,
12 are the most commonly used treatments, despite their numerous hazardous side
13 effects.

14 In the last decade, new technologies have been developed in order to resolve
15 these issues. In the magnetic therapy the drugs are guided directly into the
16 interested organs, reducing the drug absorption in the tissues which are not
17 interested by the tumor. Lungs represent an ideal target for drug delivery, due
18 to the direct access and the large area exposed to drugs [3]. Different types of
19 nanoparticles to enhance drug delivery have been studied in [4]. Mouse lungs
20 have been investigated in [5] where a large number of leukocytes have been
21 found in the lungs parenchyma and in the bronchiole lumen, suggesting they
22 were attracted by the magnetic nanoparticles present.

23 Several Computational Fluid Dynamics (CFD) studies have been carried out
24 to investigate blood flow [6–12] and the effect of nanoparticles embedded in the
25 air flow. Nano and micro particles deposition, after the construction of idealized
26 airway geometries, have been studied in [13] in order to find the optimal particle
27 diameter for drug targeting. The transport and deposition of nanoparticles for
28 cyclic and steady flow at low Reynolds numbers, have been studied in [14] by
29 evaluating the mass transfer due to nanoparticles dispersion. The inspiratory
30 flow in a three-generation symmetric bifurcation, under the assumption of low
31 Reynolds numbers has been investigated in [15], while the turbulent flow has
32 been investigated with the $k - \omega$ model in [16]. Two breathing conditions, the
33 resting/normal and the maximal one, have been studied in [17] by employing
34 a patient specific geometry. The secondary flow fields and the inertial effects
35 in patient specific lung geometries, obtained from Computed Tomography (CT)
36 data set has been studied in [18]. Other studies focused on subject specific
37 boundary conditions [19] and on the application of CFD to the surgery field
38 in order to evaluate the flow rates in patients with bidirectional anastomosis
39 [20]. The particle deposition in the lungs has been investigated in [21], by using
40 two different geometry models in order to analyze the best regions where the
41 deposition mechanism was higher.

42 Biological effects of electromagnetic fields have been investigated in [22],
43 while the application of the magnetic technique for the transport of drugs and
44 tracers in specific targets has been developed in [23]. Few CFD studies have
45 been conducted to simulate the magnetic drug targeting in blood vessels both
46 in idealized [24–27] and patient-specific [28, 29] geometries. A mathematical
47 model has been proposed in [30] in order to investigate the deposition of mag-
48 netic particles aerosol in lung alveolus, by considering only one alveolus with a
49 simplified spherical geometry. A particles diameter of $5\mu m$ and a quadrupolar
50 Halbach permanent magnet array have been used for that study.

51 The present study investigates the fluid dynamics of air inside the lower
52 respiratory tract, where nanoparticles, used for drug targeting, are aerosolized,
53 inhaled and dragged from the trachea to the bronchiole by an external mag-
54 netic field. A patient-specific geometry is reconstructed from a data set of CT
55 scan images of a middle-aged healthy man. The air is treated as a continuum
56 medium with an Eulerian formulation, while a Lagrangian approach is used for
57 the nanoparticles. A rectangular coil is the source of the external magnetic field
58 with a current intensity which complies with the clinical standards. The results
59 of the simulations without and with the magnetic probe are compared.

60 2. Materials and Methods

61 2.1. Domain reconstruction

62 The domain's geometry is generated with the open-source software VMTK
63 (The Vascular Modeling Toolkit) [31], which reconstructs a real chest surface,
64 with the trachea and its primary and secondary bronchi, from a DICOM series
65 of images. The lungs are divided into left and right, which can be further
66 divided into upper, lower and central lobes. The geometry takes into account
67 the principal and secondary bronchial tubes, belonging to the upper and central
68 lobes of the right lung, whereas the interested regions of the left one are located
69 in the lower lobe. The magnetic field is applied to the upper lobe of the right
70 lung, where the tumor is supposed to be. Because of the chest geometry, the axis
71 of the magnetic probe is directed towards the left side of the abdomen. Since
72 the procedure is operator-dependent, the non-interesting structures and artifacts
73 are removed manually. The *Level Set* algorithm is applied to reconstruct the
74 surface of interest [32, 33], which is refined with the *Parametric Deformable*
75 *Models*, initialized with the *Colliding Front* methodology. The output of the
76 *Level Set* algorithm is an image, and the *Marching Cubes* algorithm is used to
77 reconstruct the surface, due to the depth of the interested geometry.

78 Flow extensions of cylindrical shape, equal to 6 times its diameter, are added
79 to the inlets and the outlets of the domain to ensure that the flow, entering and
80 leaving the computational domain, is fully developed. This approach allows to
81 use standard boundary conditions (BC) to solve the partial differential equations
82 (PDE) governing the phenomenon. The computational grid is generated once
83 the flow extensions are added. An adaptive mesh is employed with a more refined
84 grid close to the wall and in the smaller branches. The computational grid
85 employs tetrahedral elements, with minimum and maximum dihedral angles,
86 set up in order to reduce the skew angle and the number of non-orthogonal
87 cells. Four grids are generated with different number of elements, respectively
88 144,712 (grid1), 514,723 (grid2), 853,982 (grid3) and 1,245,423 (grid 4), to verify
89 that the numerical solutions are grid-independent [15, 16].

90 The domain is shown in Fig.(1), where Fig.(1,a) presents the reconstruction
91 obtained with the application of the Marching Cubes algorithm, while Fig.(1,b)
92 labels the segments whose drug uptake is monitored during the numerical sim-
93 ulations.

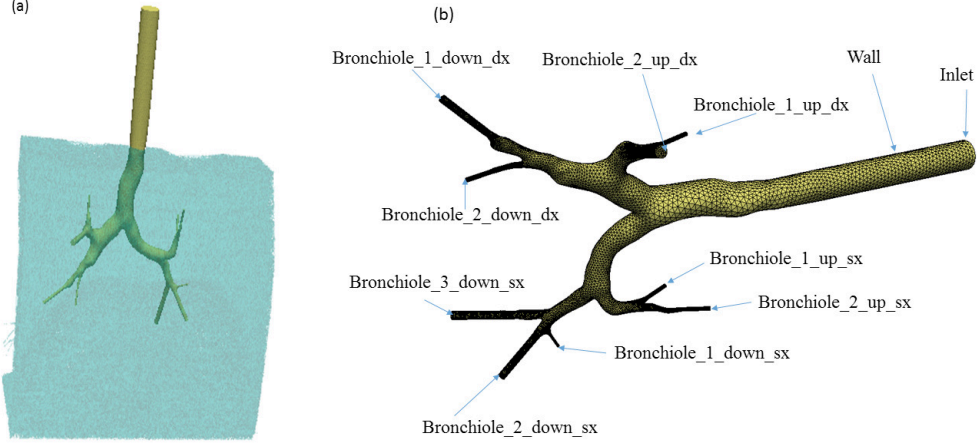


Figure 1: (a) Application of the Marching Cubes algorithm to obtain a reconstruction of the Trachea with its collateral structures; (b) Detail of the geometry used in this study.

94 2.2. Eulerian Model

95 The Magneto Hydro Dynamic (MHD) mathematical description is based on
 96 the coupling between the Navier-Stokes and the Maxwell equations. The MHD
 97 equations can be written for incompressible flow of air as follows:

$$\operatorname{div}(\vec{v}_a) = 0 \quad (1)$$

$$\frac{\partial \vec{v}_a}{\partial t} + (\vec{v}_a \cdot \nabla) \vec{v}_a = -\frac{1}{\rho_a} \nabla p + \nu_a \nabla^2 \vec{v}_a + \vec{g} + \frac{1}{\rho_a \mu_0} \operatorname{curl}(\vec{B}) \times \vec{B} \quad (2)$$

$$\frac{\partial \vec{B}}{\partial t} + (\vec{v}_a \cdot \nabla) \vec{B} = (\vec{B} \cdot \nabla) \vec{v}_a + \frac{1}{\sigma_a \mu_0} \nabla^2 \vec{B} \quad (3)$$

98 where the subscript a denotes “air”, ν_a is the kinematic viscosity, ρ_a the density,
 99 μ_0 the magnetic permeability in the vacuum, σ_a the electric conductivity,
 100 \vec{g} the gravity acceleration, p the static pressure, \vec{v}_a the velocity field, and \vec{B} the
 101 magnetic induction field. As above mentioned, the air has been considered as
 102 an incompressible fluid. This is due to the fact that in physiological condition
 103 the velocity of the air is much smaller than the speed of sound and therefore
 104 the Mach number is much smaller than 1, and the fluid can be considered in-
 105 compressible [34].

106 The air-momentum equation, Eq.(2), does not take into account the particles-
 107 air momentum transfer, because for particle volume fraction smaller than 10^{-6}

108 the disperse phase does not influence the continuum face, in agreement with
 109 [35, 36]. The effect of the magnetic field on the free ions and the erythrocytes
 110 is taken into account by the Lorentz force in Eq.(2).

111 The particle diameter used in this work is 5nm, which is typical of gold/iron-
 112 oxide nanoparticles [37, 38], and the particle geometry is spherical. Other shapes
 113 can be used, and their effect on the fluid flow is documented in the literature
 114 [39–41], but they are not considered here, because the Lagrangian model used
 115 is not suitable for non-spherical particles.

116 2.3. Lagrangian Model

117 Let us consider a particle of diameter d_p , velocity \vec{v}_p , and mass m_p , whose
 118 center position is \vec{x}_p . In a Lagrangian frame of reference, the position of each
 119 particle is obtained by the integration of its velocity,

$$\frac{d\vec{x}_p}{dt} = \vec{v}_p \quad (4)$$

120 which is evaluated from the momentum conservation equation, written as

$$\begin{aligned} \frac{d\vec{v}_p}{dt} = & - \underbrace{\frac{1}{\tau_p} \left(\vec{v}_p - \vec{v}_a + \frac{d_p^2}{12} \nabla^2 \vec{v}_a \right)}_{(I)} + \underbrace{\left(1 - \frac{\rho_a}{\rho_p} \right) \vec{g}}_{(II)} + \underbrace{\frac{\rho_a}{\rho_p} \left(\frac{\partial \vec{v}_a}{\partial t} + (\vec{v}_a \cdot \nabla) \vec{v}_a \right)}_{(III)} + \\ & \underbrace{\frac{1}{2} \frac{\rho_a}{\rho_p} \left(\frac{\partial \vec{v}_a}{\partial t} + (\vec{v}_a \cdot \nabla) \vec{v}_a - \frac{d\vec{v}_p}{dt} \right)}_{(IV)} + \underbrace{\left(\frac{q_p}{m_p} \vec{v}_p - \frac{1}{\rho_p \mu_0} \text{curl}(\vec{B}) \right)}_{(V)} \times \vec{B} \end{aligned} \quad (5)$$

121 where $\rho_p = 6m_p/\pi d_p^3$, (I) is the drag, (II) the buoyancy, (III) the carrier
 122 phase inertia, (IV) the added mass and (V) the Lorentz force. The particle-
 123 particle interactions is neglected in Eq.(5) because of the small volume of the
 124 particles, which reduces the probability of collision. Furthermore, q_p is the
 125 electric charge of the particle and τ_p the relaxation time, defined as

$$\tau_p = \frac{4}{3} \frac{\rho_p d_p}{\rho_b C_d |\vec{v}_b - \vec{v}_p|} \quad (6)$$

126 The standard definition of the drag coefficient, according to [42], is the fol-
 127 lowing

$$C_d = \begin{cases} \frac{24}{\text{Re}_p} & \text{Re}_p < 0.1 \\ \frac{24}{\text{Re}_p} \left(1 + \frac{1}{6} \text{Re}_p^{2/3} \right) & 0.1 < \text{Re}_p < 1000 \\ 0.44 & \text{Re}_p > 1000 \end{cases} \quad (7)$$

128 where the particle Reynolds number is defined as

$$\text{Re}_p = \frac{d_p |\vec{v}_b - \vec{v}_p|}{\nu_b} \quad (8)$$

129 *2.4. Boundary Conditions (BC)*

130 The solution of the Eulerian system requires appropriate boundary condi-
 131 tions (BC). A non-slip BC is imposed for the velocity on the wall. As far as the
 132 outlets are concerned, a mixed BC is employed: when the air leaves the domain
 133 the velocity normal derivative is set to zero, whereas the tangential velocity is
 134 set to zero when air enters through the boundary. The velocity profile is imposed
 135 on the inlet with a parabolic profile in steady state, while a Womersley-Evans
 136 profile is employed in unsteady state, in analogy with [10, 29],

$$v_a(t, \xi) = 8 \frac{Q}{\pi D^2} (1 - \xi^2) + 2\Re \left(\sum_{n=1}^N V_n \Phi(\tau_n, \xi) e^{j\omega_n t} \right) \quad (9)$$

137 where

$$\Phi(\tau_n, \xi) = \frac{J_0(\tau_n) - J_0(\tau_n \xi)}{J_0(\tau_n) - 2J_1(\tau_n)/\tau_n} \quad (10)$$

138 and

$$\tau_n = j^{\frac{3}{2}} \frac{D}{2} \sqrt{\frac{\rho}{\mu_\infty} \omega_n} = j^{\frac{3}{2}} \alpha_n \quad (11)$$

139 Being r the radial coordinate, D the tracheal diameter, Q the volumetric flow
 140 rate, $\xi = 2r/D$, J_0 and J_1 the zeroth and first-order Bessel functions of the first
 141 kind, α_n the Womersley numbers of order n , $\Re()$ the real part of a complex
 142 number, $j = \sqrt{-1}$, V_n the Fourier coefficients of the pulsatile mean velocity
 143 profile and the number of harmonics used to reproduce the flow rate. By using
 144 the Fast Fourier Transform (FFT) algorithm, the first ten Fourier coefficients
 145 of the flow rate in the trachea, derived from experimental data [17–19], are
 146 employed to reconstruct the velocity profile.

147 The physiological waveform is reported in Fig.(2). The flow rate is pulsatile
 148 and the Reynolds number varies from 0 to 2536, meaning that the flow is lam-
 149 inar mostly and becomes transitional only at the peaks of the inhalation and
 150 exhalation phases. For this reason the flow is treated as laminar, in agreement
 151 with [14, 15].

152 As far as the pressure in the unsteady state is concerned, the resistive BC,
 153 derived in [9, 20], is imposed on all the outlets

$$p = p_a + RQ \quad (12)$$

154 being p_a the reference pressure in the alveoli and R the hydraulic resistance.
 155 The value of the resistance and the reference pressure are extrapolated from
 156 the steady state simulations by imposing the volumetric flow rates and a zero
 157 normal derivative condition for the pressure on the outlets.

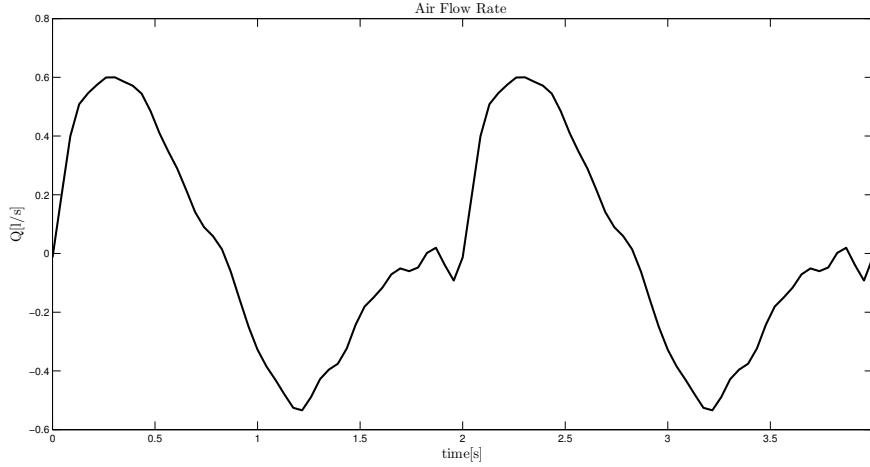


Figure 2: Pulmonary Flow Rate vs time.

158 *2.5. Magnetic Induction BC*

159 The Boundary Conditions for the magnetic induction field are zero normal
 160 derivatives everywhere, except on the wall, where the magnetic field of the probe
 161 is imposed. The external magnetic field is generated by a single rectangular coil,
 162 with a negligible cross section of the wire, where an electric current is flowing.
 163 This single rectangular coil is quite common in the clinical practice [43–46].

164 An analytical expression for the magnetic induction field is derived in [47].
 165 A point in the coil reference frame, whose origin is at its centre, is identified
 166 by the coordinates (x', y', z') . The coil dimensions are $2a_1$ along the x' axis
 167 and $2b_1$ in the y' direction, with a section of 2.5cm^2 . The axis is normal of the
 168 coil surface. The axis z' is normal of the coil surface. The components of the
 169 magnetic induction field are

$$B_{x'} = \frac{\mu_0 I_1}{4\pi} \sum_{a=1}^4 \left[\frac{z'(-1)^{a+1}}{r_a [r_a + d_a]} \right] \quad (13)$$

$$B_{y'} = \frac{\mu_0 I_1}{4\pi} \sum_{a=1}^4 \left[\frac{z'(-1)^{a+1}}{r_a [r_a + C_a(-1)^{a+1}]} \right] \quad (14)$$

$$B_{z'} = \frac{\mu_0 I_1}{4\pi} \sum_{a=1}^4 \left[\frac{d_a(-1)^a}{r_a [r_a + C_a(-1)^{a+1}]} - \frac{C_a}{r_a [r_a + d_a]} \right] \quad (15)$$

170 with

<i>Normal</i>	<i>CoilCoords(m)</i>	<i>TargetCoords(m)</i>	$\vec{B} _{1cm}(\text{mT})$
$n_x = -0.082166$	$x_c = -0.054377$	$x_t = 0.0314$	0
$n_y = 0.93057$	$y_c = -0.0891$	$y_t = -0.3554$	0
$n_z = 0.35677$	$z_c = -0.21683$	$z_t = 0.9342$	46.21

Table 1: Source and target coordinates; values for the normal to the chest surface of the patient; intensity of the Magnetic field along the z' - axis.

$H_D(\text{cm})$	$W_D(\text{cm})$	$D_D(\text{cm})$	$D_{M-T}(\text{cm})$	$T_O(\text{s})$	Re_{\max}
31.6	10.0	2.0	12.32	2.0	2536

Table 2: Simulation Parameters: H_D (domain height), W_D (domain width), D_D (domain depth), D_{S-T} (magnet-tumor distance), T_O (observation time), Re_{\max} (max tracheal Reynolds number).

$$\left\{ \begin{array}{l} C_1 = -C_4 = a_1 + x' \\ C_2 = -C_3 = a_1 - x' \\ d_1 = d_2 = y' + b_1 \\ d_3 = d_4 = y' - b_1 \\ r_a = \sqrt{C_a^2 + d_a^2 + z'^2} \end{array} \right. \quad (16)$$

171 The magnetic probe is located 1cm above the patient skin, in order that its
172 modulus is smaller than 1.5 T. This is the limit allowed in clinical treatments
173 [3, 4], since higher values can cause damage to the patient. The centre of the
174 probe and the target are aligned with the z' axis. The target of the magneto-
175 therapy is located at the upper lobe of the right lung because the maximum
176 magnetic field must be concentrated on it.

177 The external chest surface of the patient is reconstructed using VMTK, with
178 the procedure previously illustrated for the trachea. Two geometries are located
179 in the same reference frame, in order to calculate the coordinates of the probe
180 and the target. The dimensions of the rectangular coil, the current intensity
181 and the positions of coil and target are reported in Tab.(1), while the main
182 simulation parameters are listed in Tab.(2).

183 2.6. Numerical Details

184 The numerical simulations are performed with the software OpenFOAM,
185 which solves the governing equations through the Finite Volume Method (FVM).
186 The present problem has been solved with the `mhdB4Foam` solver, developed in
187 [29], which couples the Lagrangian particle dynamics with the Eulerian MHD.
188 Some Boundary Conditions, such as the resistive BC, the pulsatile profile on
189 the inlet for unsteady state and the parabolic profile for steady state, are imple-
190 mented through the utility `groovyBC`, in analogy with [29]. Furthermore, the

191 imposed magnetic field on the domain has been set using the `rectMagProbe`
 192 external OpenFOAM module, developed in [29]. The simulations are carried on
 193 for 2 respiratory cycles, considering a period of 1s and a variable time step, in
 194 order to guarantee a Courant number smaller than 0.5 during the respiratory
 195 cycle.

196 3. Results and Discussion

197 3.1. Steady State

198 The steady state simulations are carried out until convergence is reached with
 199 the `simpleFoam` solver of OpenFOAM, which solves the Navier-Stokes equations
 200 in steady state. The numerical results, obtained with the four meshes, grid1,
 201 grid2, grid3 and grid4, are compared by using the `mapFields` utility, which maps
 202 the fields from one grid to another. The wall shear stress (WSS), defined as

$$\tau_{wall} = \hat{i}_{axis} \cdot \rho_a \nu_a ([I] - \hat{n}_{wall} \otimes \hat{n}_{wall}) \left([\nabla \vec{v}_a] + [\nabla \vec{v}_a]^T - \frac{2}{3} \text{div}(\vec{v}_a) [I] \right)_{wall} \hat{n}_{wall} \quad (17)$$

203 is used to evaluate the grid independence. The contours of WSS are shown in
 204 Fig.(3). The WSS does not change significantly from grid1 to grid4. Therefore,
 205 grid2 is employed to perform the unsteady simulations, being a compromise
 206 between speed of execution and accuracy.

207 Figure 3 shows smaller WSS in the Trachea, due to the small velocity gradi-
 208 ent, growing in the primary bronchi and reaching the maximum in the secondary
 209 bronchi. At the entrance of the secondary bronchi, the WSS increases, due to
 210 the section reduction. In a circular pipe the WSS is inversely proportional to
 211 the cubed radius. The increased number of branches reduces the mean velocity,
 212 which tends to reduce the WSS as well. However, the section reduction be-
 213 tween primary and secondary bronchi is such that the WSS increases, despite
 214 the smaller mean velocity in the branches.

215 3.2. Unsteady State without external magnetic field

216 The unsteady state simulations, without external magnetic field, are carried
 217 out by imposing the value of the current intensity to zero. As far as the inlet
 218 velocity is concerned, a pulsatile velocity profile is imposed. Figure 4 shows the
 219 time variations of the pressure field, on the domain wall, at four different time
 220 steps of the respiratory cycle.

221 The pressure variations during the respiratory cycle are very small, about
 222 1 cm of H₂O. During the inhalation there is a net flux of air to the lungs,
 223 as consequence of the reverse pressure gradient directed from the environment
 224 to the lungs, which decreases the pressure from the trachea to the secondary
 225 bronchi, as shown in Fig.(4,a). At the end of the inhalation, there is no net
 226 mass flow of air between lungs and environment, and the pressure is uniform, as
 227 shown in Fig.(4,b). At the end of the inspiratory phase, Fig.(4,c), the pressure

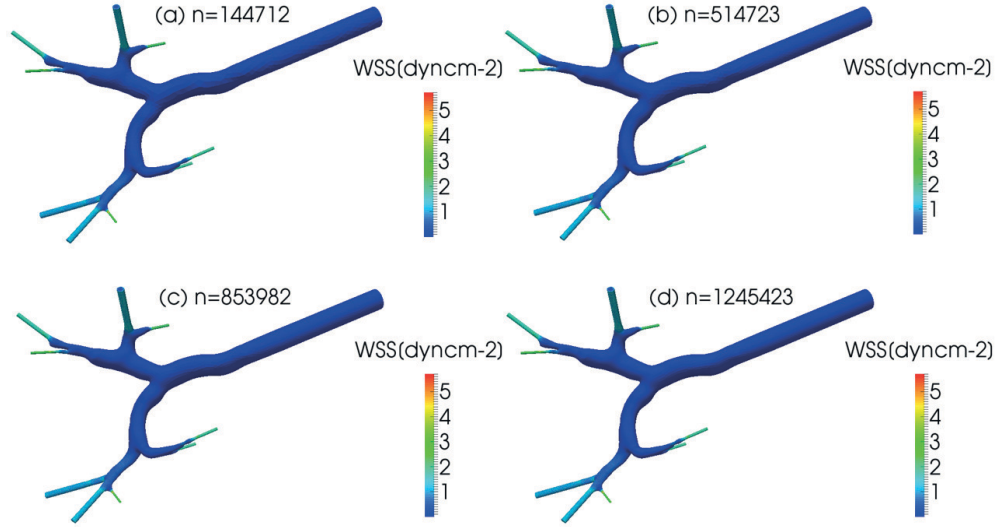


Figure 3: WSS field for the grid independence study in steady state conditions.

228 increases slightly. At the beginning of the exhalation, a reverse pressure gradient
 229 is established between the trachea and the secondary bronchi and air is exhaled,
 230 as shown in Fig.(4,d).

231 Figure 5 presents the nanoparticles coloured by their speed modulus. In
 232 Fig.(5,a-b) shows a parabolic-like profile at the beginning of the inhalation,
 233 confirming the laminar regime of motion, is shown. The particles with high
 234 speed leave the trachea reaching the bronchi, while the particles with low velocity
 235 tend to move towards the wall, where they are adsorbed. The adsorption of
 236 magnetic nanoparticles in bronchiole lumen has been observed in animal studies
 237 [5]. The particles adhesion to the wall is favoured by the low flow rate during
 238 the exhalation phase, as confirmed by Fig.(5,d-f).

239 3.3. Unsteady State with external magnetic field

240 The results of the particle motion in the respiratory system with the mag-
 241 netic probe turned on are presented in this section. The position of the coil and
 242 the target, the probe direction and the intensity of the magnetic induction field,
 243 evaluated at 1 cm from the center of the coil, are reported in Table 1.

244 The maps of the magnetic field on the wall of the lower respiratory tract are
 245 shown in Figure ?? at different time steps from the beginning, up to the end

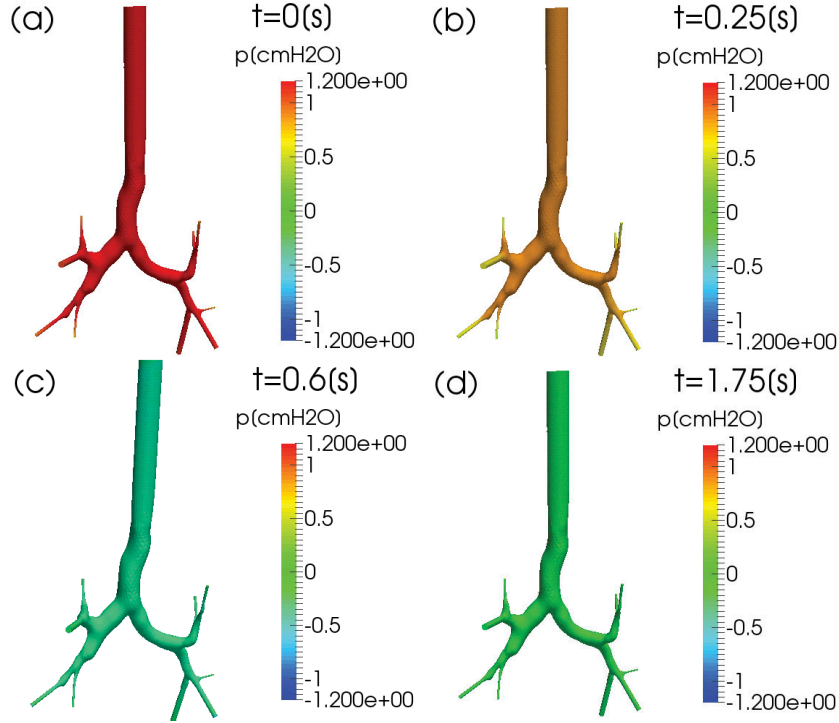


Figure 4: Unsteady Pressure field at different time-steps in absence of external magnetic field.

246 of the exhalation process, when the particles have filled the entire domain. The
 247 maximum value of the magnetic induction field is located on the closer branch
 248 to the right upper lobe, where the probe is located, and where the particles tend
 249 to be dragged.

250 The particles path-lines at six instants of time are reported in Figure 7,
 251 showing that the flow is transitional. At the beginning of the inhalation, the
 252 path-lines are mostly straight, with the presence of few vortexes, especially
 253 near the bifurcations, where the velocity gradient becomes higher because of
 254 the cross-section reduction. The highest velocity is reached in the trachea,
 255 where the environmental air enters into the lungs. Intermittent vortexes form
 256 near the bifurcations, due to the curvature changes. At the beginning of the
 257 exhalation phase, Fig.(7,b-f), the flow rate is lower and directed towards the
 258 trachea, promoting an helical flow with highly tangled path-lines. With this
 259 flow-field the time that the particles spend close to the lower respiratory tract
 260 wall increases, promoting adsorption. Since the tumor is located in the upper
 261 right lobe of the lungs the increased wall adsorption ultimately reduces the
 262 efficiency of the technique.

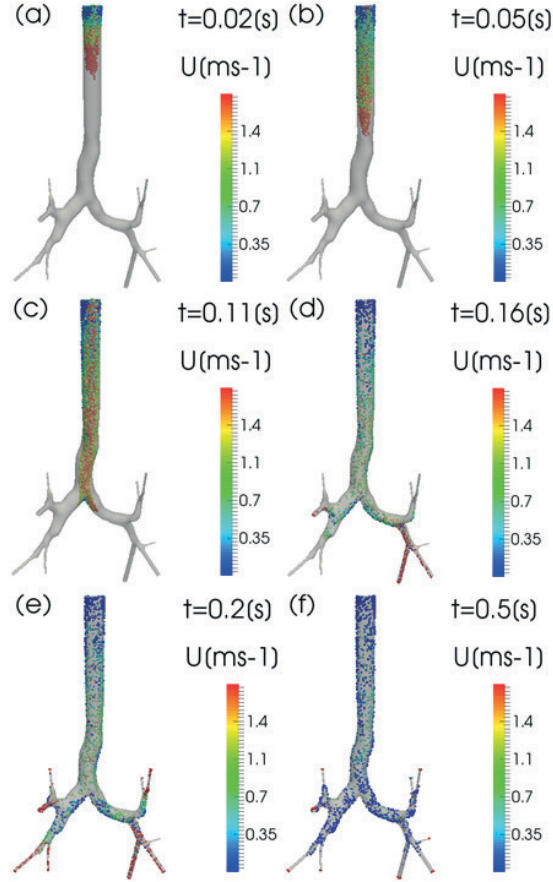


Figure 5: Particles speed at different time-steps in absence of external magnetic field.

263 Figures 8 and 9 show the influence of the magnetic field on the particles
 264 absorption. In order to underline the effect of the magnetic field, the results
 265 with the magnetic probe turned off are reported as well.

266 Figure 8 reports the particle flow rate per unit volume on the different bound-
 267 aries during the respiratory cycle. In the Trachea and on the domains wall the
 268 particle flow rates are of the same order of magnitude. The peak of the ex-
 269 halation process occurs between 1s and 1.4 s, when the highest flow rate from
 270 the lungs to the environment occurs. Figures (9,b,e,f,h,j), show that this phase
 271 corresponds to an increase in particle uptake in bronchioles, probably due to the
 272 formation of several low speed recirculation regions during the exhalation. The
 273 geometry of the bronchi is such that their diameter decreases as they proceed
 274 from the trachea to the alveoli. Therefore, since during exhalation the air moves

275 from the alveoli to the trachea, a flow detachment occurs, causing recirculation
276 regions and promoting the uptake of nanoparticles.

277 Since the particle flow rate may not show the effectiveness of the use of a
278 rectangular coil in the magnetic targeting, its time integration, corresponding
279 to the total number of particles that crosses a given section from the beginning
280 of the process, is performed.

281 The probe is pointed towards the upper right lobe of the patients lungs.
282 The uptake of nanoparticles increases in the branches of the lower respiratory
283 tract bended in the frontal direction, Fig.(9,b,e,f,h,j), while it decreases in the
284 branches bended towards the spine, Fig.(9,c,d,g,i). A slight reduction in the
285 particles adhesion to the domain wall is also evidenced.

286 Despite the increase of particles concentration in the targeted regions, shown
287 in Fig.(9,b), the effect of the magnetic field is not significant. More than 50%
288 of the injected particles adhere to the domain wall when the magnetic probe is
289 turned off, while it is only 47%, when the magnetic probe is turned on. Similarly,
290 the increase of the nanoparticles in the different regions is less than 1%.

291 This behavior can be due to the high surface-volume ratio of the lower respi-
292 ratory tract, which inherently increases the probability of adhesion, regardless
293 of the intensity of the magnetic field, and to the geometry of the probe. The
294 magnetic field on the axis of a single square loop decreases quickly from its
295 origin, about 100 times at a distance equal to 2.5 times its width. Considering
296 that the distance between the source and the target is about 12.32 cm, it is clear
297 that this makes the modulus of the magnetic induction considerably low.

298 4. Conclusions

299 The present work investigates the dynamics of nanoparticles in air flow dur-
300 ing magnetic therapy of a lung tumor, which is an emerging alternative to
301 chemotherapy, because of the reduced side effects. At the best of the authors
302 knowledge, this work represents the first numerical investigation of this tech-
303 nique in a patient-specific lower respiratory tract. The lack of numerical studies
304 is probably due to the complexity of the problem, which couples the air flow
305 with the nanoparticles dynamics under the influence of an external magnetic
306 field. The purpose of this work is to verify numerically the effectiveness of this
307 technique in the treatment of lung cancer. As every numerical study, this work
308 is subject to the limitations due to the input parameters and the model chosen.

309 The numerical simulations, for steady and unsteady flow, are carried out
310 with the OpenFOAM code in laminar flow, in agreement with [14, 15], with
311 Newtonian viscosity for the air and absence of inter and intraparticle forces,
312 due to the small size of the drug carriers. The simulations are performed in
313 a patient specific geometry, reconstructed from CT slices with VMTK. Three
314 routines are employed in OpenFOAM to implement the BCs for the resistive
315 pressure, the periodic pulsatile velocity profile and the magnetic field from the
316 rectangular coil. Furthermore, a solver coupling the Eulerian MHD of the air
317 with the Lagrangian motion of particles is developed.

318 One simulation with the magnetic probe turned off and one with the probe
319 turn on are carried out. The results are compared to assess the increase of drug
320 uptake in the lung due to the magneto-therapy and consequently the reduced
321 dispersion in other locations. The rectangular coil, pointing perpendicularly to
322 the tumor is positioned in a specific point, 1 cm above the upper right lobe of
323 the lungs.

324 The results of the numerical simulations show that, despite the induced
325 magnetic field increases the particle uptake, a small fraction of the total number
326 of particles injected reaches the target. This can be due to the high surface
327 volume ratio of the lower respiratory tract and the design of the magnetic probe.

328 This conclusion is in contrast with the mathematical model developed for
329 lung alveolus in [30]. This is probably due to the different probe employed, the
330 larger particle diameter ($5 \mu m$) and the higher magnetic field (0.2-2.2 T). Mag-
331 netic drug delivery is extremely sensitive to these parameters. Moreover, the
332 drug distribution in different branches is not investigated in [30]. The low per-
333 formance of the magnetic drug delivery in the present study can be due to three
334 factors: (i) the nanoparticle size; (ii) the magnet-tumor distance; (iii) the probe
335 design. As far as the nanoparticle size is concerned, as shown by Eqs.(18,19) in
336 [29] a low particle diameter increases the acceleration due to Lorentz force, but
337 it also increases the friction. However, because of the low magnetic field applied
338 [48, 49] the effect on the friction is predominant. Therefore, larger particles
339 should increase the effectiveness of the technique, as in [30]. The probe-tumor
340 distance is another factor, which limits the effectiveness of the technique. Un-
341 fortunately, this parameter cannot be tuned at will, and in a superficial tumor,
342 the magnetic drug targeting is likely be more effective.

343 The design of the magnetic probe is another factor that influences the out-
344 come of the procedure. The modulus of the magnetic induction field of a single
345 rectangular coil decreases considerably with the distance from the target, as in
346 the right lung. Being the right lung about 12.32 cm far from the source, the
347 modulus of the magnetic induction field is considerably small. A solution to this
348 problem could be to increase the value of the current intensity flowing in the
349 probe, but this is not possible because higher values of the magnetic field could
350 affect the health of the patient, and is forbidden by law [48, 49]. A solution
351 could be to modify the design of the probe in order to reduce the rate of decay
352 of the magnetic field. A possible configuration could include multiple probes,
353 positioned in appropriate locations.

354 CFD allows detailed visualization of biological fluid flows, which increases
355 our understanding of natural phenomena, but it has some limitations due to
356 computational resources required to simulate a process in a complex domain.
357 The question then rises as to whether or not the observation time (2 s) is
358 sufficient to judge the effectiveness of the technique. It would be certainly better
359 to extend the simulations to few minutes, but the particle volumetric flow rate
360 in Fig. 9 show negligible differences between the cases. It seems unlikely that
361 the percentage of injected particles, which reach the right lung will significantly
362 increase over time.

363 Further numerical simulations, in different patient-specific geometries and

364 with different probes, are planned to assess the effectiveness of the therapy in
365 different conditions.

366 5. Acknowledgments

367 This research did not receive any specific grant from funding agencies in the
368 public, commercial, or not-for-profit sectors. The authors thank the staff of the
369 Policlinico di Tor Vergata for the support with the biomedical images.

370 References

- 371 [1] D. M. Parkin, F. Bray, J. Ferlay, P. Pisani, Global cancer statistics, 2002,
372 CA: a cancer journal for clinicians 55 (2005) 74–108.
- 373 [2] I. Globocan, Estimated cancer incidence, mortality and prevalence world-
374 wide in 2012, 2012, (accessed 18 November 2017). [http://globocan.iarc.
375 fr/Pages/fact_sheets_cancer.aspx](http://globocan.iarc.fr/Pages/fact_sheets_cancer.aspx).
- 376 [3] N. Labiris, M. Dolovich, Pulmonary drug delivery. part i: physiological fac-
377 tors affecting therapeutic effectiveness of aerosolized medications, British
378 journal of clinical pharmacology 56 (2003) 588–599.
- 379 [4] V. Chandolu, C. R Dass, Treatment of lung cancer using nanoparticle drug
380 delivery systems, Current drug discovery technologies 10 (2013) 170–176.
- 381 [5] M. P. Garcia, R. M. Parca, S. B. Chaves, L. P. Silva, A. D. Santos, Z. G. M.
382 Lacava, P. C. Morais, R. B. Azevedo, Morphological analysis of mouse lungs
383 after treatment with magnetite-based magnetic fluid stabilized with dmsa,
384 Journal of magnetism and magnetic materials 293 (2005) 277–282.
- 385 [6] F. Gori, A. Boghi, M. Amitrano, Three-dimensional numerical simulation of
386 the fluid dynamics in a coronary stent, in: ASME International Mechanical
387 Engineering Congress and Exposition, Proceedings, volume 2, 2009, pp.
388 407–411.
- 389 [7] F. Gori, A. Boghi, Image-based computational fluid dynamics in a carotid
390 artery, in: ASME International Mechanical Engineering Congress and Ex-
391 position, Proceedings, volume 2, 2009, pp. 123–128.
- 392 [8] F. Gori, A. Boghi, Three-dimensional numerical simulation of non-
393 newtonian blood in two coronary stents, in: 2010 14th International Heat
394 Transfer Conference, American Society of Mechanical Engineers, 2010, pp.
395 109–114.
- 396 [9] F. Gori, A. Boghi, Three-dimensional numerical simulation of blood flow
397 in two coronary stents, Numerical Heat Transfer, Part A: Applications 59
398 (2011) 231–246.

- 399 [10] A. Boghi, F. Gori, Numerical simulation of blood flow through different
400 stents in stenosed and non-stenosed vessels, *Numerical Heat Transfer, Part*
401 *A: Applications* 68 (2015) 225–242.
- 402 [11] I. Di Venuta, A. Boghi, F. Gori, Three-dimensional numerical simulation
403 of a failed coronary stent implant at different degrees of residual stenosis.
404 part i: Fluid dynamics and shear stress on the vascular wall, *Numerical*
405 *Heat Transfer, Part A: Applications* 71 (2017) 638–652.
- 406 [12] A. Boghi, I. Di Venuta, F. Gori, Three-dimensional numerical simulation
407 of a failed coronary stent implant at different degrees of residual stenosis.
408 part ii: Apparent viscosity and wall permeability, *Numerical Heat Transfer,*
409 *Part A: Applications* 71 (2017) 653–665.
- 410 [13] C. Kleinstreuer, Z. Zhang, Z. Li, Modeling airflow and particle trans-
411 port/deposition in pulmonary airways, *Respiratory physiology & neurobi-*
412 *ology* 163 (2008) 128–138.
- 413 [14] Z. Zhang, C. Kleinstreuer, Airflow structures and nano-particle deposition
414 in a human upper airway model, *Journal of computational physics* 198
415 (2004) 178–210.
- 416 [15] Y. Liu, R. So, C. Zhang, Modeling the bifurcating flow in an asymmetric
417 human lung airway, *Journal of biomechanics* 36 (2003) 951–959.
- 418 [16] H. Luo, Y. Liu, Modeling the bifurcating flow in a ct-scanned human lung
419 airway, *Journal of Biomechanics* 41 (2008) 2681–2688.
- 420 [17] R. Calay, J. Kurujareon, A. E. Holdø, Numerical simulation of respiratory
421 flow patterns within human lung, *Respiratory physiology & neurobiology*
422 130 (2002) 201–221.
- 423 [18] J. De Backer, W. Vos, C. Gorle, P. Germonpré, B. Partoens, F. Wuyts,
424 P. M. Parizel, W. De Backer, Flow analyses in the lower airways: patient-
425 specific model and boundary conditions, *Medical engineering & physics* 30
426 (2008) 872–879.
- 427 [19] Y. Yin, J. Choi, E. A. Hoffman, M. H. Tawhai, C.-L. Lin, Simulation of
428 pulmonary air flow with a subject-specific boundary condition, *Journal of*
429 *biomechanics* 43 (2010) 2159–2163.
- 430 [20] G. Pennati, C. Corsini, D. Cosentino, T.-Y. Hsia, V. S. Luisi, G. Du-
431 bini, F. Migliavacca, Boundary conditions of patient-specific fluid dynamics
432 modelling of cavopulmonary connections: possible adaptation of pulmonary
433 resistances results in a critical issue for a virtual surgical planning, *Interface*
434 *Focus* 1 (2011) 297–307.
- 435 [21] N. Nowak, P. P. Kakade, A. V. Annapragada, Computational fluid dynam-
436 ics simulation of airflow and aerosol deposition in human lungs, *Annals of*
437 *biomedical engineering* 31 (2003) 374–390.

- 438 [22] W. R. Adey, Biological effects of electromagnetic fields, *Journal of cellular*
439 *biochemistry* 51 (1993) 410–416.
- 440 [23] Z. Saiyed, S. Telang, C. Ramchand, Application of magnetic techniques
441 in the field of drug discovery and biomedicine, *BioMagnetic Research and*
442 *Technology* 1 (2003) 1–8.
- 443 [24] M. Larimi, A. Ramiar, A. Ranjbar, Numerical simulation of magnetic
444 nanoparticles targeting in a bifurcation vessel, *Journal of Magnetism and*
445 *Magnetic Materials* 362 (2014) 58–71.
- 446 [25] M. D. Tehrani, J.-H. Yoon, M. O. Kim, J. Yoon, A novel scheme for
447 nanoparticle steering in blood vessels using a functionalized magnetic field,
448 *IEEE Transactions on Biomedical Engineering* 62 (2015) 303–313.
- 449 [26] M. Larimi, A. Ramiar, A. Ranjbar, Numerical simulation of magnetic
450 drug targeting with eulerian-lagrangian model and effect of viscosity mod-
451 ification due to diabetics, *Applied Mathematics and Mechanics* 37 (2016)
452 1631–1646.
- 453 [27] M. Momeni Larimi, A. Ramiar, A. A. Ranjbar, Magnetic nanoparticles
454 and blood flow behavior in non-newtonian pulsating flow within the carotid
455 artery in drug delivery application, *Proceedings of the Institution of Me-*
456 *chanical Engineers, Part H: Journal of Engineering in Medicine* 230 (2016)
457 876–891.
- 458 [28] S. Kenjereš, B. Righolt, Simulations of magnetic capturing of drug carriers
459 in the brain vascular system, *International Journal of Heat and Fluid Flow*
460 35 (2012) 68–75.
- 461 [29] A. Boghi, F. Russo, F. Gori, Numerical simulation of magnetic nano drug
462 targeting in a patient-specific coeliac trunk, *Journal of Magnetism and*
463 *Magnetic Materials* 437 (2017) 86–97.
- 464 [30] A. Krafcik, P. Babinec, I. Frollo, Computational analysis of magnetic field
465 induced deposition of magnetic particles in lung alveolus in comparison to
466 deposition produced with viscous drag and gravitational force, *Journal of*
467 *Magnetism and Magnetic Materials* 380 (2015) 46–53.
- 468 [31] D. A. Steinman, Image-based computational fluid dynamics modeling in
469 realistic arterial geometries, *Annals of biomedical engineering* 30 (2002)
470 483–497.
- 471 [32] L. Antiga, B. Ene-Iordache, L. Caverni, G. P. Cornalba, A. Remuzzi, Geo-
472 metric reconstruction for computational mesh generation of arterial bifur-
473 cations from ct angiography, *Computerized Medical Imaging and Graphics*
474 26 (2002) 227–235.

- 475 [33] L. Antiga, M. Piccinelli, L. Botti, B. Ene-Iordache, A. Remuzzi, D. A.
476 Steinman, An image-based modeling framework for patient-specific com-
477 putational hemodynamics, *Medical & biological engineering & computing*
478 46 (2008) 1097–1112.
- 479 [34] D. F. Young, B. R. Munson, T. H. Okiishi, W. W. Huebsch, A brief intro-
480 duction to fluid mechanics, John Wiley & Sons, 2010.
- 481 [35] S. Elghobashi, On predicting particle-laden turbulent flows, *Applied sci-
482 entific research* 52 (1994) 309–329.
- 483 [36] E. Tzirtzilakis, V. Sakalis, N. Kafoussias, P. Hatzikonstantinou, Biomag-
484 netic fluid flow in a 3d rectangular duct, *International Journal for Numerical
485 Methods in Fluids* 44 (2004) 1279–1298.
- 486 [37] M. Arruebo, R. Fernández-Pacheco, M. R. Ibarra, J. Santamaría, Magnetic
487 nanoparticles for drug delivery, *Nano today* 2 (2007) 22–32.
- 488 [38] S. Seino, Y. Matsuoka, T. Kinoshita, T. Nakagawa, T. A. Yamamoto,
489 Dispersibility improvement of gold/iron-oxide composite nanoparticles by
490 polyethylenimine modification, *Journal of Magnetism and Magnetic Materi-
491 als* 321 (2009) 1404–1407.
- 492 [39] M. Hassan, A. Zeeshan, A. Majeed, R. Ellahi, Particle shape effects on
493 ferrofluids flow and heat transfer under influence of low oscillating magnetic
494 field, *Journal of Magnetism and Magnetic Materials* 443 (2017) 36–44.
- 495 [40] A. Zeeshan, M. Hassan, R. Ellahi, M. Nawaz, Shape effect of nanosize
496 particles in unsteady mixed convection flow of nanofluid over disk with
497 entropy generation, volume 231, SAGE Publications Sage UK: London,
498 England, 2017, pp. 871–879.
- 499 [41] A. Majeed, A. Zeeshan, T. Hayat, Analysis of magnetic properties of
500 nanoparticles due to applied magnetic dipole in aqueous medium with mo-
501 mentum slip condition, *Neural Computing and Applications* (2017) 1–9.
- 502 [42] L. Schiller, Z. Naumann, A drag coefficient correlation, *Vdi Zeitung* 77
503 (1935) 51.
- 504 [43] G. J. Metzger, P.-F. van de Moortele, C. Akgun, C. J. Snyder, S. Moeller,
505 J. Strupp, P. Andersen, D. Shrivastava, T. Vaughan, K. Ugurbil, et al.,
506 Performance of external and internal coil configurations for prostate inves-
507 tigations at 7 t, *Magnetic resonance in medicine* 64 (2010) 1625–1639.
- 508 [44] F. Dughiero, E. Baake, M. Forzan, V. Nemkov, R. Ruffini, R. Goldstein,
509 J. Jackowski, T. DeWeese, R. Ivkov, Magnetic field generating inductor
510 for cancer hyperthermia research, *COMPEL - The international journal
511 for computation and mathematics in electrical and electronic engineering*
512 30 (2011) 1626–1636.

- 513 [45] A. S. Lübbe, C. Alexiou, C. Bergemann, Clinical applications of magnetic
514 drug targeting, *Journal of Surgical Research* 95 (2001) 200–206.
- 515 [46] A. S. Lübbe, C. Bergemann, H. Riess, F. Schriever, P. Reichardt,
516 K. Possinger, M. Matthias, B. Dörken, F. Herrmann, R. Gürtler, et al.,
517 Clinical experiences with magnetic drug targeting: a phase i study with 4-
518 epidoxorubicin in 14 patients with advanced solid tumors, *Cancer research*
519 56 (1996) 4686–4693.
- 520 [47] M. Misakian, Equations for the magnetic field produced by one or more
521 rectangular loops of wire in the same plane, *Journal of research of the*
522 *National Institute of Standards and Technology* 105 (2000) 557–564.
- 523 [48] E. Council, Recommendation on the limitation of exposure of the general
524 public to electromagnetic field (0 hz to 300 ghz), *Official Journal of the*
525 *European Communities* 199 (1999) 59–70.
- 526 [49] F. C. Commission, Evaluating compliance with FCC guidelines for human
527 exposure to radiofrequency electromagnetic fields, volume 65, *OET Bulletin*,
528 1997.

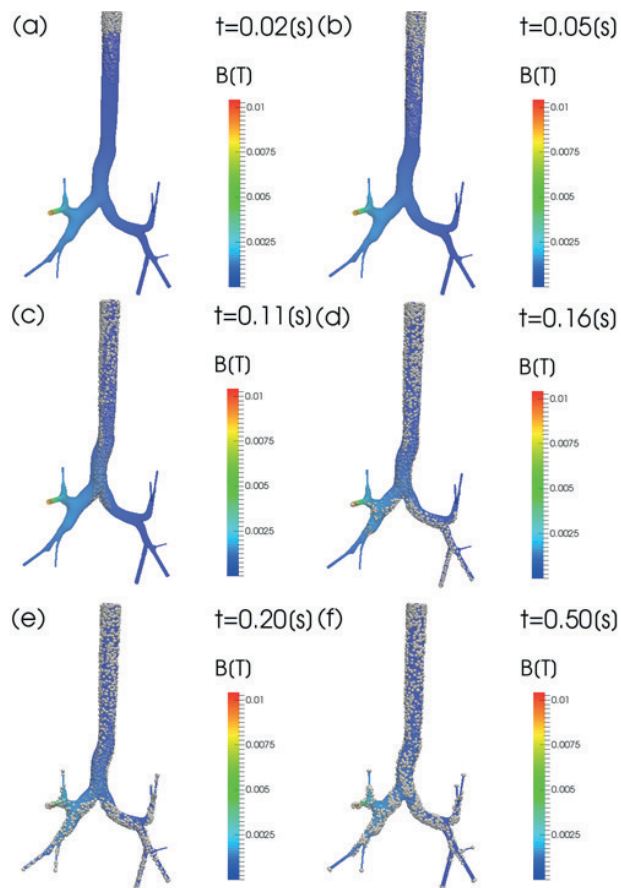


Figure 6: Magnetic Induction Field and particle positions at different time steps, with external magnetic field.

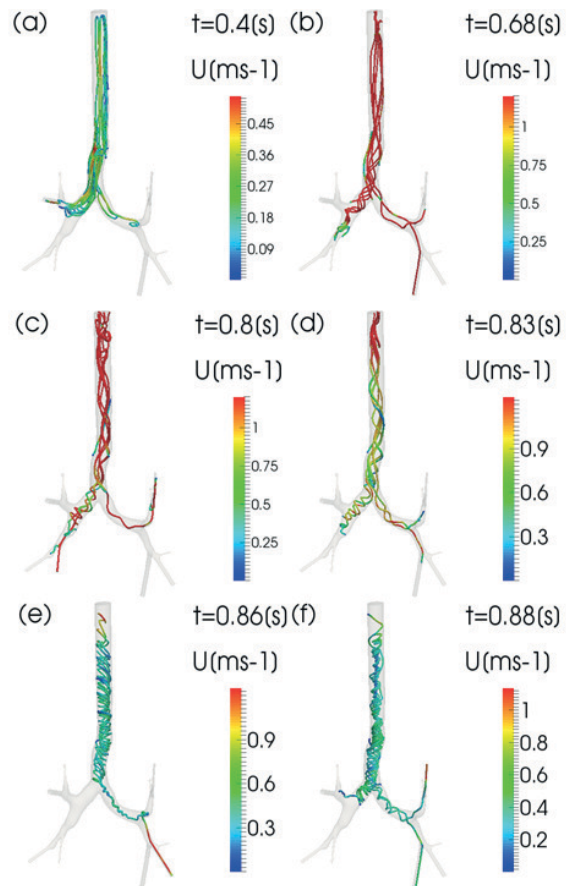


Figure 7: Velocity Field and velocity streamlines at different time steps with external magnetic field.

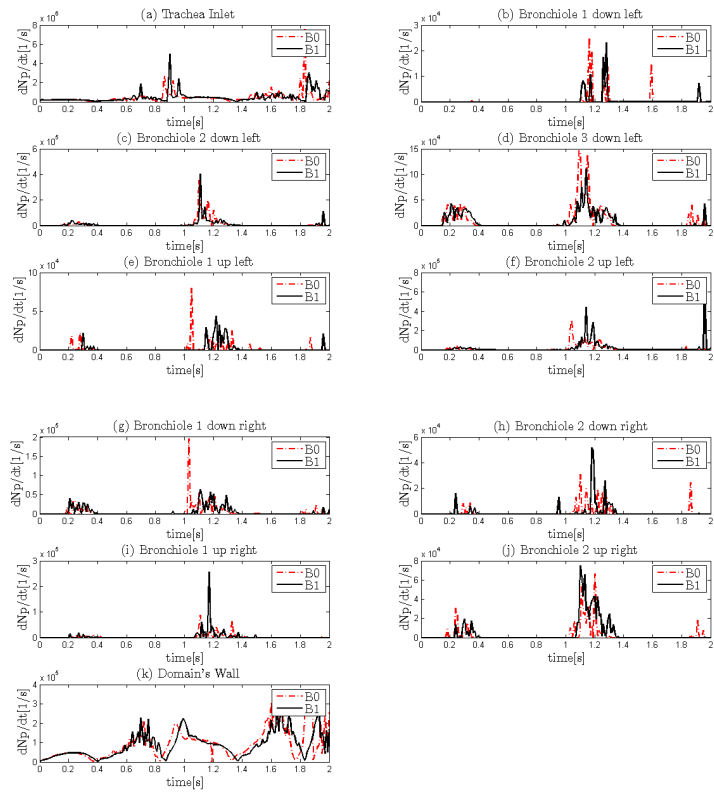


Figure 8: Particle volumetric flow rate per unit volume vs time for the two different conditions. B0 = magnetic field off; B1 = magnetic field on.

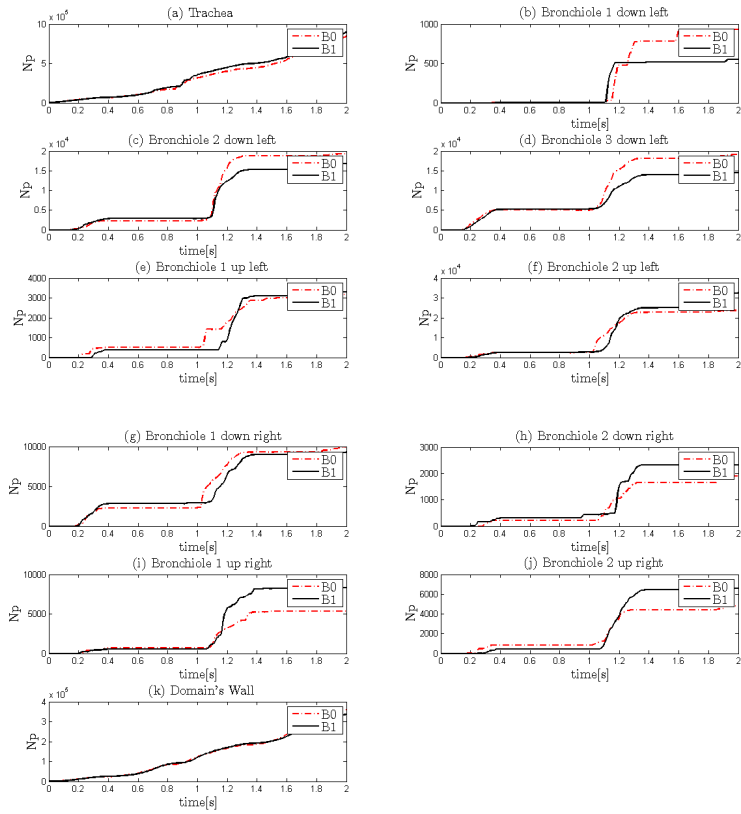


Figure 9: Particle number vs time for the two different conditions. B0 = magnetic field off; B1 = magnetic field on.